Int. J. Electrochem. Sci., 13 **(2018)** 1640 – 1655, doi: 10.20964/2018.02.43

International Journal of
ELECTROCHEMICAL
SCIENCE
www.electrochemsci.org

Study on the in Vitro Degradation Behavior of Commercial Zn–4%Al–Sr Alloy for Biomedical Applications

Yang Liu[1,3,4], Zhongyi Yin[1], Yue Liu[1], Cong Geng[1,3], Xu Chen[2,], Junrui Xu[1,*] and Jinfeng Peng[1]*

[1] School of Mechanical Engineering, Xiangtan University, Xiangtan 411105, China
[2] School of Materials Science and Engineering, Xiangtan University, Xiangtan 411105, China
[3] Key Laboratory of welding robot and application technology of Hunan Province, Xiangtan University, Xiangtan411105, China
[4] Engineering Research Center of Complex Tracks Processing Technology and Equipment of Ministry of Education, Xiangtan University, Xiangtan41105, China
[*]E-mail: chenxusun@163.com, xujunrui_hit@163.com

Received: 29 August 2017 / *Accepted:* 8 December 2017 / *Published:* 28 December 2017

Zn and Zn-based alloys have been recognized as potential biodegradable materials, due to their proven biocompatibility and lower corrosion rates compared to Mg alloys. However, pure Zn has poor mechanical properties while Zn–4wt.% Al alloy (Zn–4Al) degrades in a nonuniform manner. In this study, Sr was used as a promising alloying element to improve the uniform corrosion properties of Zn–4Al alloy. Microstructure and in vitro degradation behavior of Zn–4Al alloys with addition of different concentrations of Sr (0–0.15 wt%) were systematically investigated. Increasing Sr addition progressively decreased the volume fraction of primary η-Zn phase and progressively increased the (β+η) lamellar eutectic morphology. The alloy with 0.1 wt% Sr displayed the best corrosion resistance. Most importantly, the Zn–4Al–0.1Sr alloy exhibited a more uniform corrosion mode in Hanks' solution, which could reduce stress concentration and rapid reduction in the mechanical integrity.

Keywords: Biodegradable metals; Zn-based alloys; strontium; corrosion behavior

1. INTRODUCTION

Biodegradable metals (BMs) have broad applications in orthopedic implants and cardiovascular interventional devices, owing to a good combination of biodegradable property and biocompatibility [1, 2]. During the last decade, magnesium (Mg), iron (Fe) and their alloys have been widely studied as biodegradable metals [3-7]. Mg-based biodegradable metals display a rapid corrosion rate without effective support after being implanted in the body, while Fe-based biodegradable metals slowly degrade at a rate similar to permanent implants [6-8].

Zn and Zn-based alloys have more appropriate degradation rates that are close to clinical requirements because their standard potential is between that of Mg and Fe [9]. Furthermore, Zn is an essential element in the human body; it is involved in various aspects of cellular metabolism and is required by many transcription factors. It plays an important role in immune functions, and protein and DNA syntheses as three examples. [10]. The recommended daily intake of Zn ranges from 10 mg for adults to 2-3 mg for infants, with an upper limit of 8-11 mg [11]. Aside from being physiologically essential, Zn exhibits strong anti-atherogenic properties by preventing metabolic physiologic derangements of the vascular endothelium [12]. But, pure Zn has poor mechanical strength, which must be improved to satisfy the requirements for clinical applications [13, 14].

Generally, mechanical properties of metallic materials are modified by adding alloying elements [15-17]. Alloying elements must be carefully selected to be benign in terms of biocompatibility. Research interest has focused on pure Zn and Zn alloys with nutrient elements like Mg and Ca [18]. Little attention has been given to commercial Zn-Al alloys. In contrast to novel Zn-X(Mg, Ca) alloys, commercial Zn-Al alloys have attractive physical and mechanical properties including excellent cast ability, high strength and promising plasticity [19, 20]. Unfortunately, excessive Al is harmful to neurons, bone and osteoblasts [21], and has been associated with dementia [22, 23] and Alzheimer's disease [24]. However, commercial alloys containing limited amounts of Al or other potentially harmful elements remain worth studying as potential candidates for biomedical applications [25]. For example, commercial Mg-Al alloys, such as AZ and WE alloy series, have been widely studied as biodegradable metals [26-28]. The first clinical study of a Mg alloy coronary stent involved WE43 alloys [29]. Therefore, commercial Zn-Al alloys containing limited amounts of Al can also be regarded as novel and potentially biodegradable metals. Nevertheless, Zn-Al alloys can easily develop severe pitting corrosion in simulated human body environments due to the nonuniform distribution of second phases, which cause a rapid reduction in the mechanical integrity during the degradation process.

Strontium (Sr) is an essential element in the human body. Sr plays a special role in bone remodeling, and is associated with the inhibition of bone resorption and the stimulation of bone formation [30]. Thus, Sr is thought to be effective in enhancing the bioactivity and biocompatibility of biomaterials. We previously investigated the effect of Sr on the microstructure and mechanical properties of Zn–4Al alloy [31]. The mechanical properties of Zn–4Al alloys increased with increasing Sr content, peaking at 0.1 wt%. However, the effect of Sr on the uniform corrosion behavior of Zn–4Al alloys was not completely elucidated.

In this paper, the effect of Sr content on the uniform corrosion behavior of commercial Zn–4Al alloys in Hanks' solution was studied. The uniform corrosion behavior of these alloys were determined, with special emphasis on the corrosion rate, corrosion product composition and corrosion morphology. The results of our investigation will be important biodegradable applications of novel Zn-based alloys.

2. EXPERIMENTAL

2.1. Materials

Pure Zn (99.995%), pure Al (99.995%), pure Mg (> 99.9%) and Zn-8.55% Sr master alloy were melted in a graphite crucible furnace with protection of CO_2. Degassing was carried out with zinc chloride (0.15wt %). After about 30 min holding and stirring, the molten alloy was poured into a permanent mould preheated at 200 ^{o}C. The analyzed chemical compositions of the investigated alloys are given in Table 1, as measured by inductively coupled plasma-atomic emission spectroscopy (ICP-AES).

Table 1. Chemical composition of the experimental Zn–4Al alloys and the Sr contents (wt %).

Alloy	Al	Mg	Sr	Zn
Alloy 1	4.02	0.048	0	Bal.
Alloy 2	3.96	0.049	0.033	Bal.
Alloy 3	3.95	0.048	0.062	Bal.
Alloy 4	4.05	0.046	0.102	Bal.
Alloy 5	4.06	0.051	0.153	Bal.

2.2. Microstructure characterizations

Microstructure characterization and compositions of experimental alloys were carried out by Sirion200 back-scattered scanning electron microscopy (BSEM) equipped with energy dispersive spectroscopy (EDS). The phases were further analyzed by SIMENSD 500 type analyzer (XRD) at 40kV and 45mA.

2.3. Immersion test

Immersion tests were performed in Hanks' solution simulated body fluid (NaCl 8.0 g,$CaCl_2$ 0.14 g, KCl 0.4 g, $NaHCO_3$ 0.35 g, glucose 1.0 g, $MgCl_2{\cdot}6H_2O$ 0.1 g, $Na_2HPO_4{\cdot}2H_2O$ 0.06 g, KH_2PO_4 0.06 g, $MgSO_4{\cdot}7H_2O$ 0.06 g dissolved in 1 L deionized water) at 37 ± 1 °C according to ASTM-G31-72 [32]. The samples were immersed in the solution for (1, 3, 5, 10, 15, 20, and 30) d. After each immersion test, the corroded specimens were rinsed with distilled water in an ultrasonic bath for 15 min to remove the corrosion products. The surface morphologies and chemical compositions of the alloys both before and after removing the corrosion products were examined by SEM and EDS. Then, the specimens were washed quickly with distilled water, dried, and then weighed again to obtain the final weight (w_1). The difference between original weight (w_0) and w_1 was designated as the corrosion weight loss (Δw).

2.4. Polarization measurement

Potentiodynamic tests were carried out with a traditional three-electrode cell using a ZAHNER Im6ex electrochemical workstation (Germany) at 37 ± 1 ℃ in Hanks' solution. The specimen, a saturated calomel electrode (SCE) and a platinum electrode were used as the working electrode, reference electrode, and the auxiliary electrode, respectively. Before potentiodynamic tests, surfaces of samples were polished. The open-circuit potential (OCP) of each sample was monitored for 6000 s. Afterwards, potentiodynamic polarization tests were carried out at a scanning rate of 1 mV/s. The tests were normally repeated two or three times. Corrosion parameters including OCP, corrosion potential (E_{corr}) and corrosion current density (I_{corr}) were analyzed by linear fit and Tafel extrapolation to the cathodic and anodic parts of polarization curves.

3. RESULTS

3.1. Microstructural characterization

According to the Zn–Al binary phase diagram as shown in Fig. 1 [33], during the solidification of casting Zn–4Al alloy, the primary η-Zn phase solidifies firstly from the melt to form the cores of dendrites. As the temperature decreases to 382 ℃ where a eutectic transformation occurs, β+η eutectic structure precipitates from the residual liquid enriched with a solute segregation. As the temperature further decreases to 275 ℃ where a eutectoid transformation occurs, the β phase decomposes to α+η eutectoid structure.

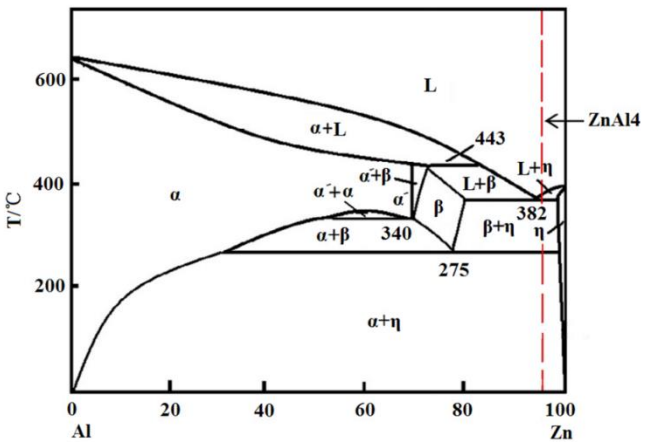

Figure 1. Zn–Al binary alloy phase diagram.

Fig. 2 shows the BSEM images of the as-cast Zn–4Al alloys with different amounts of Sr. According to Fig. 2(a), the resultant microstructure of as-cast Zn–4Al alloy mainly comprised coarse primary η-Zn phases, eutectoid structures, and lamellar eutectic (β+η) in the inter-dendrite regions. As the Sr content increased, the volume fraction and the size of primary η-Zn phase decreased, but the

amount of eutectic structure increased. When Sr content increased up to 0.1 wt %, the microstructure of the alloy mainly comprised lamellar eutectic morphology (β+η) (Fig. 2(d)). With the further increase of Sr content to 0.15 wt %, the amount of primary η-Zn phase increased and the volume fraction of the lamellar eutectic (β+η) decreased (Fig. 2(e)).

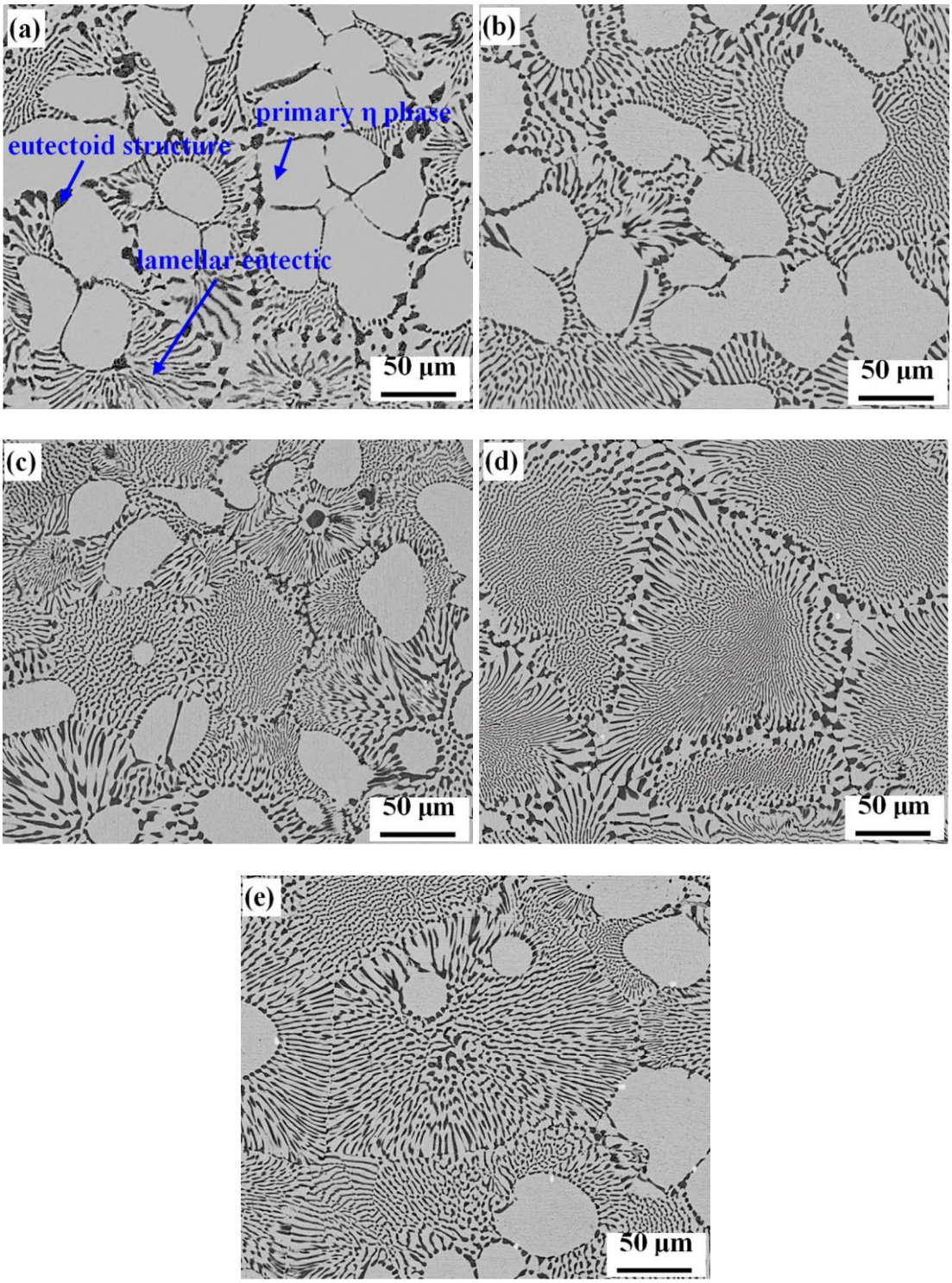

Figure 2. BSEM micrographs of as-cast Zn–4Al alloy with different amounts of Sr: (a) 0, (b) 0.03 (c) 0.06, (d) 0.1 and (e) 0.15 wt %.

The XRD patterns of Zn–4Al alloys with different amounts of Sr are shown in Fig. 3 [31]. Two phases were evident: η-Zn phase and α-Al phase in the Zn–4Al–xSr alloys. However, the β phase did not appear on the X-ray diffractogram, perhaps because the β phase completely decomposed to a (α+η) eutectoid structure. Peaks corresponding to $SrZn_{13}$ phase were observed in the alloys with 0.1 wt % Sr. The diffraction intensity of the $SrZn_{13}$ phase increased with further increase of the Sr content to 0.15 wt %. However, the $SrZn_{13}$ phase was not observed on the X-ray diffractogram when the Sr content was below 0.1 wt %, which may be because of the volume fraction of the $SrZn_{13}$ phase being below the limits detection of the XRD technique. Fig. 4 shows the BSEM images and EDS pattern of the $SrZn_{13}$ phases in sample containing 0.15 wt % Sr. Precipitates with sharp-edged or irregular structures were distributed along the primary η-Zn phase. By analyzing the corresponding EDS pattern and XRD pattern, it could be concluded that these precipitated phases were the intermetallic compound $SrZn_{13}$.

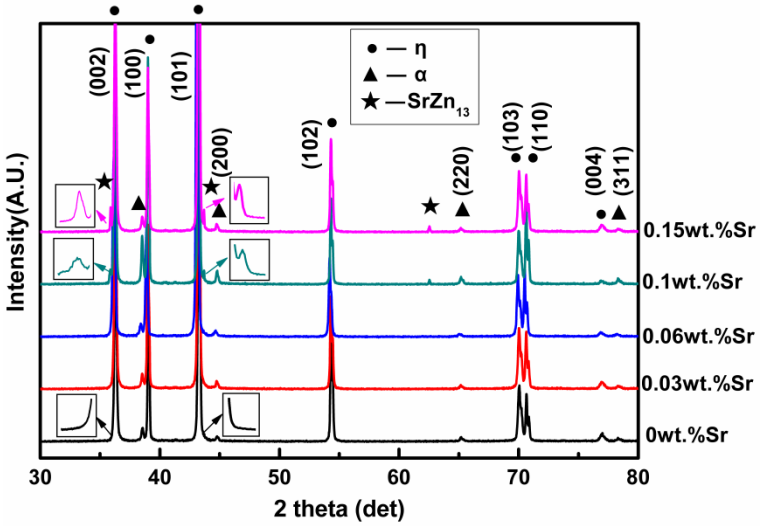

Figure 3. X-ray diffraction patterns of the Zn–4Al alloy with varying amounts of Sr [31].

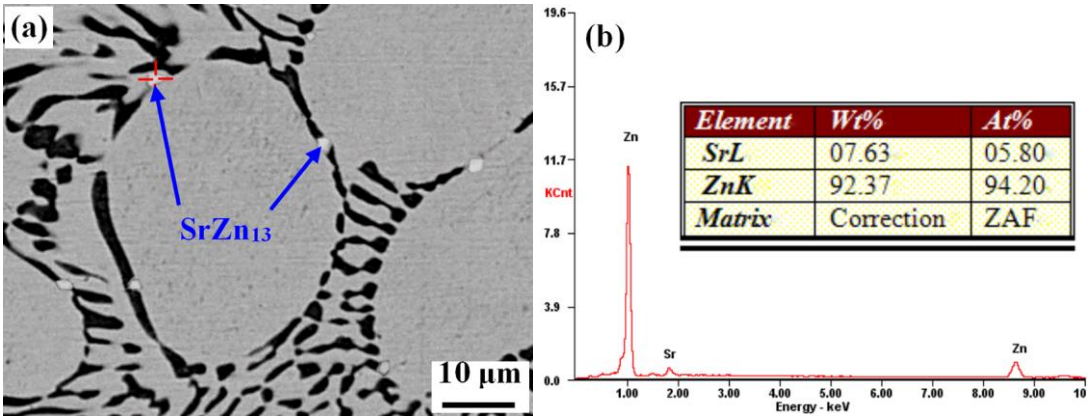

Figure 4. BSEM image and EDS analysis of $SrZn_{13}$ phase with 0.15 wt % Sr: (a) BSEM image; (b) EDS pattern of $SrZn_{13}$ phase.

3.2. Weight loss and corrosion rate

The weight loss and corrosion rate of the specimens can be calculated as follows:

$$C = \frac{w_0 - w_1}{S} \quad (1)$$

$$v = \frac{w_0 - w_1}{St} \quad (2)$$

where C represents the weight loss of metal after corrosion (g cm^{-2}), v represents the corrosion rate (g cm^{-2} d^{-1}), w_0 and w_1 are the initial weight (g) and the final weight after the removal of the corrosion products (g), respectively, S and t are the surface area (cm^2) and the immersion time (d), respectively.

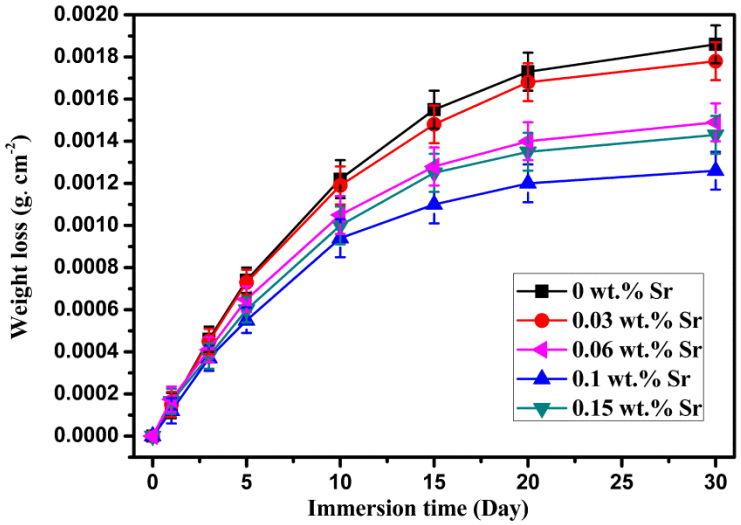

Figure 5. Weight losses of the Zn–4Al–xSr alloys after immersion in Hanks' solution for 30d varying with amounts of Sr.

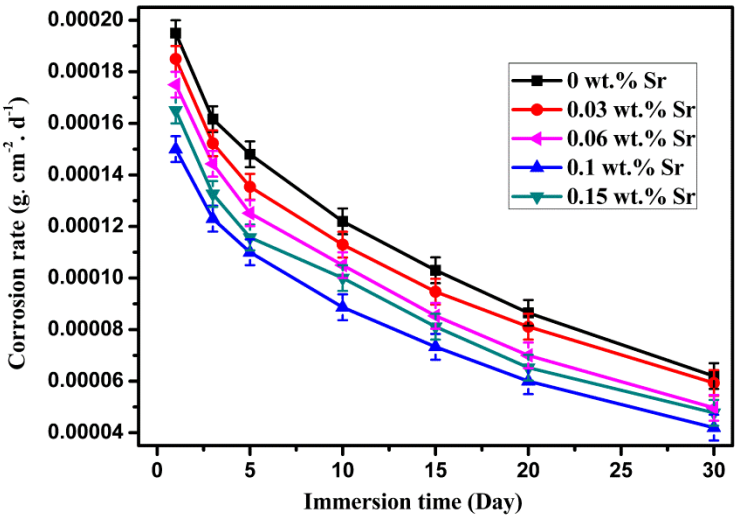

Figure 6. Corrosion rate of the Zn–4Al–xSr alloys after immersion in Hanks' solution for 30 d varying with amounts of Sr.

The values acquired for the average weight losses of the specimens are presented in Fig. 5. The average weight losses of the five samples increased with prolonged immersion time. In addition, the average weight losses decreased as the Sr content increased, where the lowest value occurred at 0.1 wt % Sr addition. A further increase in the Sr content to 0.15 wt % increased the weight losses.

Fig. 6 shows the relationship between the corrosion rate and the immersion time. The corrosion rates of the five samples decreased with immersion time. Furthermore, the corrosion rates on the immersion time vary with increasing Sr content. After the addition of 0.1 wt % Sr, the corrosion rates remarkably decreased when the alloy was immersed for 30 days. However, a further increase in Sr content increased the corrosion rates.

3.3. Polarization curves

Fig. 7 shows the polarization curves of the Zn–4Al alloys in Hanks' solution containing different amounts of Sr. The polarization characteristics of formation and breakdown of a passive film are similar among all the samples. Two current plateau existed in the polarization curves. The first current plateau was observed on the cathodic branch of polarization curves, which indicated the formation of a passive film on the surface of sample. Another passive region emerged in the anodic part of the curves before the occurrence of transpassivation. This region indicated the growth of the passive film.

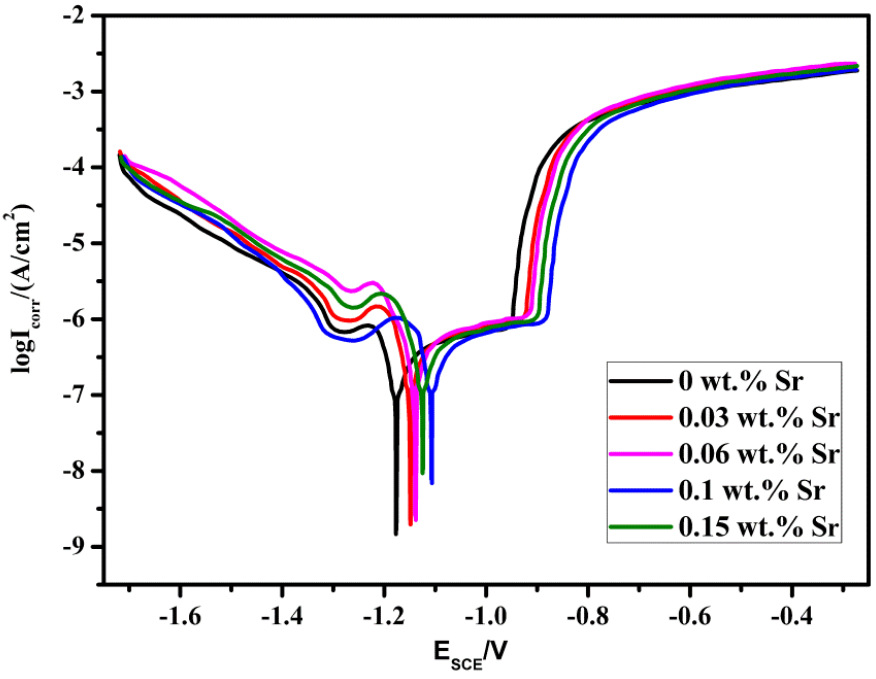

Figure 7. Polarization curves of the Zn–4Al alloys in Hanks' solution varying with amounts of Sr.

The current densities increased rapidly at nobler potentials as a result of breakdown of the passive film. Using the Tafel extrapolation method, the corrosion current density (I_{corr}) and the corrosion potential (E_{corr}) with varying amounts of Sr are calculated in Table 2. The E_{corr} of Zn–4Al–Sr alloys were higher than that of Sr-free alloy, which indicated a lower corroding tendency after the

addition of Sr. Generally, lower I_{corr} values were thought to be better resistant to corrosion or more inert. It can be seen from Table 2 that the I_{corr} varies with the lowest value (2.47 μA/cm^2) obtained in the sample with 0.1 wt % Sr and the highest value (3.97 μA/cm^2) in Sr-free alloy. Therefore, the Zn–4Al–0.1Sr alloy had the best corrosion performance among all the samples.

Table 2. Electrochemical parameter values of Zn–4Al alloys with different amounts of Sr in Hanks' solution.

Alloy	I_{corr}(μA/cm^2)	E_{corr}(mV)
Alloy 1	3.97	-1176
Alloy 2	3.26	-1148
Alloy 3	2.64	-1136
Alloy 4	2.47	-1102
Alloy 5	3.02	-1124

3.4. Corrosion morphology

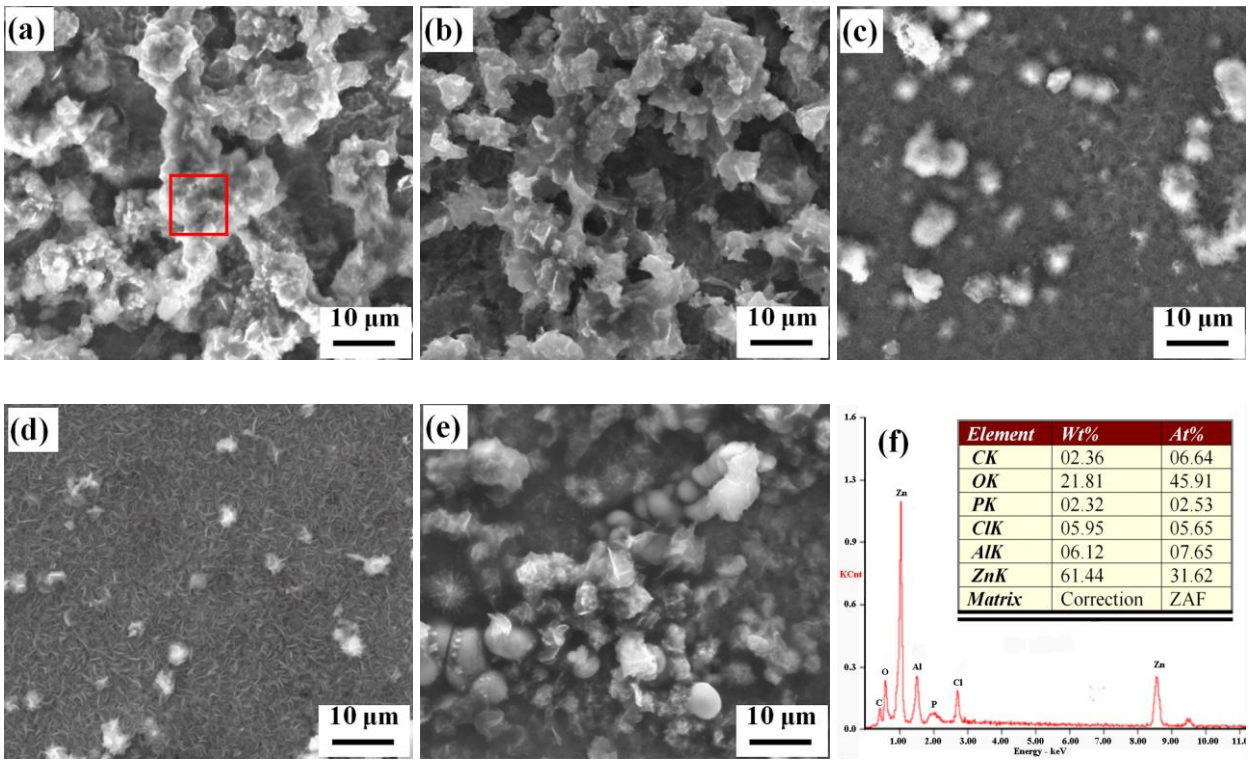

Figure 8. SEM images of the specimens immersed in Hanks' solution for 30 days before the removal of the corrosion products: (a) 0, (b) 0.03 (c) 0.06, (d) 0.1, (e) 0.15 wt % and (f) EDS result performed at red frame.

Fig. 8 shows the surface corrosion morphologies of Zn–4Al–xSr alloys immersed in the Hanks' for 30 days before the removal of the corrosion products. More looser corrosion products were observed on the surface of the Sr-free alloy (Fig. 8(a)). EDS analysis of corrosion products of Zn–4Al alloy revealed the presence of C, O, P, Cl, Al, and Zn (Fig. 8(f)). With increasing the Sr content, the corrosion products on the sample surface decreased. When the additional amount of Sr was 0.1 wt %, the corrosion products was uniform and dense that could effectively stop the invasion of corrosive medium. With further increasing the Sr content to 0.15 wt %, an accumulation of loose corrosion products appeared in several locations (Fig. 8(e)).

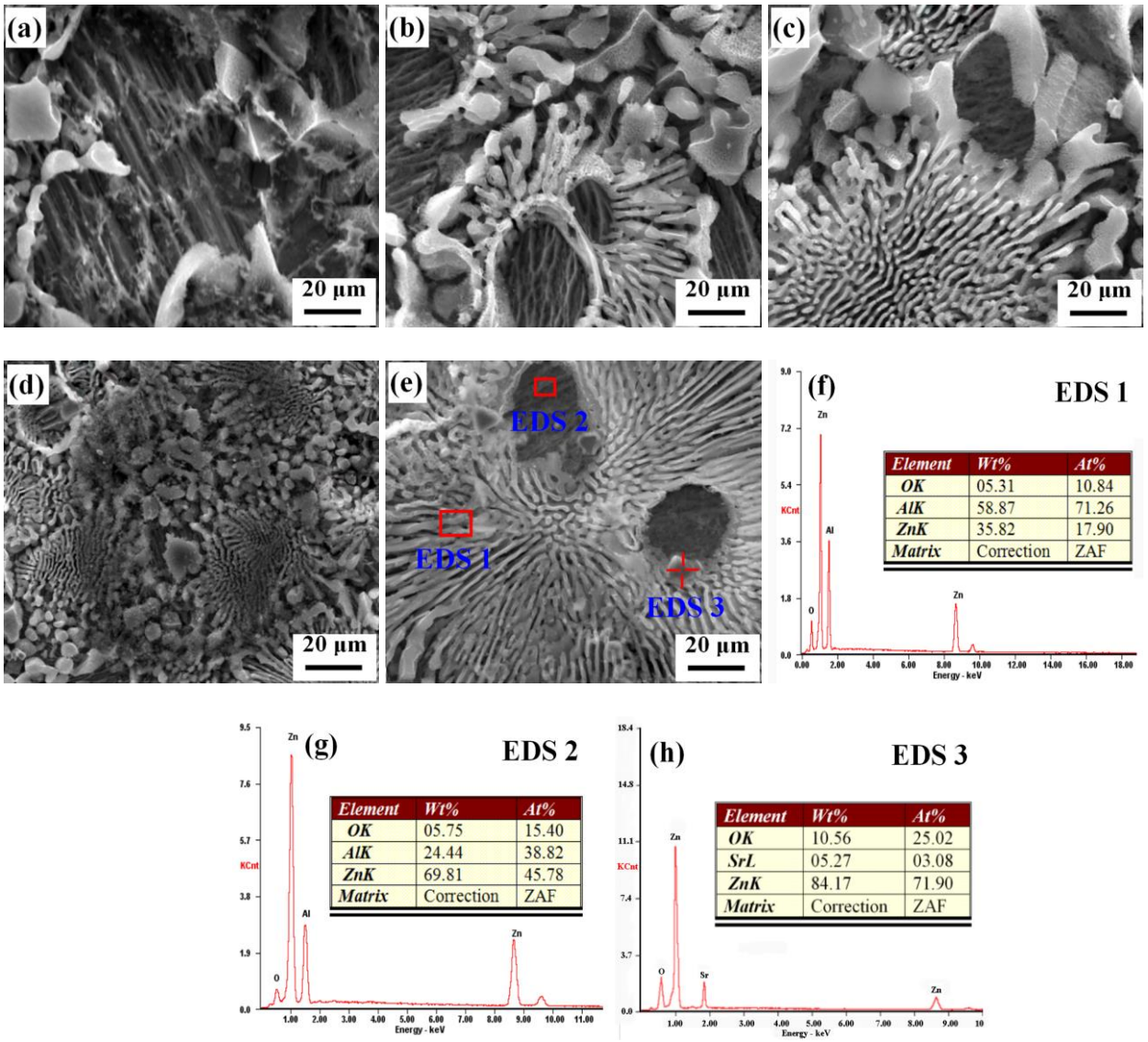

Figure 9. SEM images of the specimens immersed in the Hanks' solution for 30 days after removing the corrosion products: (a) 0; (b) 0.03; (c) 0.06; (d) 0.1; (e) 0.15 wt %. Panels (f), (g), and (h) display EDS spectra corresponding to the area marked by a red frame.

Fig. 9 shows the SEM images of the Zn–4Al alloy with different amount of Sr immersed in the Hanks' solution for 30 days after removing the corrosion products. The surfaces suffered from serious corrosion with distribution of the localized anodic main attack sites. Analyzing the corresponding EDS

pattern revealed corrosion sites with η-Zn phases stripped and β-Al phases dissolved on the surfaces. These were caused by the presence of the more active β-Al phases, resulting in galvanic corrosion reaction [25]. In addition, the dark particles with irregular structures were distributed along the pitting holes of η-Zn phase (Fig. 9(e)). The EDS pattern analysis indicated that these particles were mainly composed of Sr and Zn, as shown in Fig. 9(h). It was concluded that these particles represented the corrosion products of $SrZn_{13}$ phases.

4. DISCUSSION

4.1. The corrosion behavior of Zn–4Al–xSr alloys in Hanks' solution

Generally, the corrosion resistance of metallic material mainly depends on the alloying element, phase composition, corrosion product morphology and impurities. The standard potentials of Al and Zn are -1.662 and -0.762 V (versus SHE), respectively [34]. Therefore, the β-Al phase are tending to be more negative potential than that of η-Zn phase. The active β-Al phase is prone to corrode and the corrosion rate is higher than that in the η-Zn phase when immersed in Hanks' solution [25]. In the initial stage of corrosion, the β-Al phases are corroded by micro-galvanic coupling between β-Al and η-Zn phases, and the corrosion products mainly cover the β-Al phase. With the increment of immersion time, the whole grain is corroded, and this contributes to the formation of corrosion product layer on the surface of the alloy. The dissolution-passivation of Zn involves a number of intermediate species in Hanks' solution as follows [35, 36].

$$Zn + OH^- \leftrightarrow Zn(OH)_{ads} + e \quad (3)$$

$$Zn(OH)_{ads} + 3OH^- \leftrightarrow Zn(OH)_3^- + e(rds) \quad (4)$$

$$Zn(OH)_3^- + OH^- \leftrightarrow Zn(OH)_4^{2-} \quad (5)$$

$$Zn(OH)_4^{2-} \leftrightarrow Zn(OH)_2 + 2OH^- \quad (6)$$

$$Zn + 2OH^- \leftrightarrow Zn(OH)_2 + 2e \quad (7)$$

$$Zn + 2OH^- \leftrightarrow ZnO + H_2O + 2e \quad (8)$$

EDS analyses of the corrosion products of Zn–4%Al–xSr alloys after immersion tests (Fig. 8(f)) show C, P, O, Cl, Al and Zn. The C, O, P content may be the precipitation of phosphates, carbonates, oxides and insoluble hydroxides, respectively [13, 37]. This could be due to the ionic interaction between Zn^{2+} and various acid radicals such as HCO_3^-, HPO_4^{2-}, Cl^- in Hanks' solution [38].

In the presence of HCO_3^-, the formation of $ZnCO_3$ can take place according to the following reactions [39]:

$$ZnO + 2H^+ \leftrightarrow Zn^{2+} + H_2O \quad (9)$$

$$Zn^{2+} + H_2CO_3 \leftrightarrow ZnCO_{3(s)} + 2H^+ \quad (10)$$

It has been reported that HPO_4^{2-} ions can form insoluble phosphates, such as $ZnHPO_4$ and inhibit the dissolution of Zn [1]. Zn^{2+} may also form various soluble corrosion products, such as $ZnCl_2$ and ZnOHCl that can form the main product of $Zn_5(OH)_8Cl_2{\cdot}H_2O$. In a solution containing Cl^-, the formation of $Zn_5(OH)_8Cl_2{\cdot}H_2O$ can occur as follows [40]:

$$5ZnO + 2Cl^- + 6H_2O \leftrightarrow Zn_5(OH)_8Cl_2{\cdot}H_2O + 2OH^- \quad (11)$$

In addition, Al may contributes to the improvement of corrosion performance by the formation of Al-containing corrosion products such as $Al_2(OH)_5Cl{\cdot}2H_2O$. The corrosion products of $Al_2(OH)_5Cl{\cdot}2H_2O$ can act as a corrosion barrier which is attributed to the protective effect of the insoluble corrosion products [41].

4.2. The effect of Sr content on the corrosion kinetics of Zn–4Al alloys in Hanks' solution

According to Natesan [42], the weight loss and the immersion time is correlated by the corrosion kinetics equation

$$C = K\,t^{n} \qquad (12)$$

Where C presents the weight loss of material because of corrosion (gm^{-2}), t presents the immersion time (d) in Hanks' solution, and K and n are constants.

Taking the logarithm of both sides of Eq. (12). Then gives:

$$\log C = \log K + n \log t \qquad (13)$$

According to Eq. (13), the corrosion behavior of a certain alloy can be described by the two parameters K and n. The linear fit curves of specimens are shown in Fig. 10. A listing of K and n parameter values as well as the correlation coefficients R-squared for the Zn–4Al alloys immersed in Hanks' solution for 30 days is shown in Table.3.

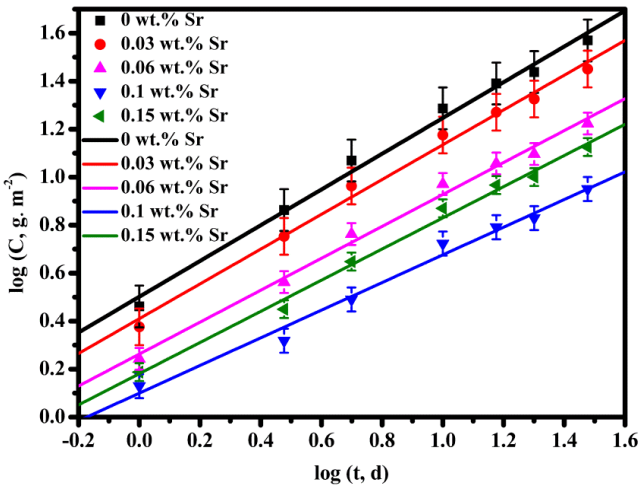

Figure 10. Log corrosion losses of the Zn–4Al alloys with varying amounts of Sr as a function of log time.

Table 3. Corrosion kinetic parameters K and n and correlation coefficient R-squared of the specimens.

Alloy	K	n	R-squared
Alloy 1	3.169	0.744	0.990
Alloy 2	2.518	0.724	0.990
Alloy 3	1.828	0.665	0.991
Alloy 4	1.256	0.576	0.984
Alloy 5	1.514	0.649	0.991

According to Eq. (13), when n = 0.5, corrosion penetration increase exhibits parabolically trend, with diffusion into the corrosion products as the rate controlling step. Lower n values (<0.5) are indicative of protective corrosion products. When n >0.5, the corrosion products show non-protective characteristics [43, 44]. In this work, the n values of all the specimens are higher than 0.5, where the n value of Zn–4Al alloy without Sr is the highest. These results indicate that the layer formed on the surface of Zn–4Al alloy is the loosest. The value of K indicates the initial corrosion rate of the specimen [45]. According to Table 3, the Zn–4Al alloy without Sr has higher initial corrosion rate than the other alloys. This may be because the volume fraction of the eutectic morphology (β+η) increases with increasing the Sr content. During corrosion, the β-Al phases may act as corrosion barriers, resulting in the decline of corrosion rate. Overall, the corrosion rate decreases with the increase of Sr content, minimum values are obtained when the additional amount of Sr is 0.1 wt %.

4.3. The effect of Sr content on the corrosion mechanism of Zn–4Al alloys in Hanks' solution

The mechanisms of Sr addition on the corrosion performance of the Zn–4Al alloy can be explained as follows. First, the amount of the (β+η) lamellar eutectic is important role in improving the corrosion performance of the Zn–4Al alloy. When η-Zn begins to dissolve, the Zn-based oxide layers are loose and non-protective in a corrosive environment [46-48]. The corrosive medium could continuously diffuse through the porous layer and react with the substrate, resulting in the extension of the galvanic reaction inward. In addition, pores can be easily blocked by the corrosion products and form an auto-catalytic corrosion cell, resulting in severe localized corrosion [18]. However, when β-Al begins to dissolve, the Al-based oxide layers are denser and finer than Zn-based oxide layers. The formation of more compact corrosion products may be responsible for the better corrosion performance. With increasing Sr content, the amount of (β+η) lamellar eutectic increases, while the volume fraction of the η-Zn phases decreases as a result of constituent supercooling [31]. In particular, the Zn–4Al–0.1Sr alloy, which has a uniform and homogeneously dispersed (β+η) lamellar eutectic morphology (Fig. 2(d)), tends to form a uniform and compact protective layer that prevent localized corrosion (Fig. 9(d)). Localized corrosion has a serious detrimental influence on the mechanical properties, which might jeopardize the integrity and normal functions of implants. Compared with the reported as-cast Zn–1.5Mg alloy, Zn–1Mg alloy and Zn–1Mg–1Sr alloy[2, 9, 18], the Zn–4Al–0.1Sr alloy possesses better uniform corrosion properties and mechanical properties. Therefore, the Zn–4Al–0.1Sr alloy can be recognized as potential biodegradable materials, due to its uniform corrosion morphologies and lower corrosion rates.

Second, the $SrZn_{13}$ phases also play a critical role in improving corrosion resistance. The $SrZn_{13}$ phases distribute discontinuously and have lower electrical potential than η-Zn phases. The $SrZn_{13}$ phases can dissolve as a sacrificial electric anode, and are expected to act as a barrier that will protect the η-Zn matrix from corrosion. Higher density of $SrZn_{13}$ phases around the η-Zn matrix can markedly improve the corrosion performance of Zn–4Al alloy. With increasing Sr content, the amount of $SrZn_{13}$ phases increases. Therefore, the Zn–4Al–0.1Sr alloy possesses the best corrosion resistance among all the samples, in which the discontinuous $SrZn_{13}$ phase acts as a sacrificial anode. The same

result was confirmed that alloying with Sr could improve the corrosion rate of Zn–1Mg alloy in Hank's solution [18]. Furthermore, the Zn–4Al–0.1Sr alloy exhibits the best mechanical properties, which mainly contribute to the increase of the eutectic fraction [31]. The findings indicate that the Zn–4Al–0.1Sr alloy can be potential candidates as biodegradable metals with a good combination of biodegradable properties and mechanical properties.

However, a further increase in the Sr content to 0.15 wt % exhibits a reduction in the corrosion performance. This could be due to a decrease in the fraction of (β+η) lamellar eutectic and an increase in the size of the primary η-Zn phase. It can be assumed that 0.1 wt % Sr is the optimum value, and that excessive Sr addition may have a detrimental influence on the corrosion performance of the Zn–4Al alloy.

5. CONCLUSION

In this work, the effect of Sr content on the uniform corrosion behavior of commercial Zn–4Al alloys have been investigated. Based on the results obtained, the following conclusions can be drawn:

1. The microstructure of Zn–4Al alloy mainly comprises coarse primary η-Zn phases, eutectoid structures and (β+η) lamellar eutectic. With increasing the Sr content, the (β+η) lamellar eutectic increases, while the size of primary η-Zn phase decreases. After the Sr content reaches 0.1 wt %, the microstructure of the alloy is mainly composed of lamellar eutectic morphology.
2. The corrosion rates on the immersion time vary with increasing Sr content. The overall corrosion rate trend is Zn–4Al > Zn–4Al–0.03Sr > Zn–4Al–0.06Sr > Zn–4Al–0.15Sr > Zn–4Al–0.1Sr.
3. A shift of corrosion regime from localized corrosion to a more uniform corrosion behavior is observed in Zn–4Al–0.1Sr alloy, mainly due to the homogenously dispersed (β+η) lamellar eutectic morphology.
4. The Zn–4Al–0.1Sr alloy possesses the best corrosion properties due to the higher volume fraction of $SrZn_{13}$ phases as well as the formation of a more compacted corrosion products on their surface.

ACKNOWLEDGEMENT
The work was funded by the National Natural Science Foundation of China (No. 51704258) and Natural Science Foundation of Hunan Province (No. 2016JJ3124 and 2016JJ3121).

References

1. E. Mostaed, M. Sikora-Jasinska, A. Mostaed, S. Loffredo, A.G. Demir, B. Previtali, D. Mantovani, R. Beanland and M. Vedani, *J. Mech. Behav. Biomed. Mater*., 60 (2016) 581.
2. X.W Liu , J.K Sun, F.Y. Zhou, Y.H Yang, R.C. Chang, K.J. Qiu, Z.J. Pu, L. Li, Y.F. Zheng, *Mater. Design*, 94 (2016) 95.
3. H.Y. Tok, E. Hamzah and H.R. Bakhsheshi-Rad, *J. Alloys Compd*., 640 (2015) 335.
4. Y. Lu, A.R. Bradshaw, Y.L. Chiu and I.P. Jones, *J. Alloys Compd*., 614 (2014) 345.
5. B. Homayun, A. Afshar, *J. Alloys Compd*., 607 (2014) 1.

6. Y. Li, C. Wen, D. Mushahary, R. Sravanthi, N. Harishankar, G. Pande and P. Hodgson, *Acta. Biomater*., 8 (8) (2012) 3177.
7. M. Schinhammer, A.C. Hanzi and P.J. Uggowitzer, *Acta. Biomater*., 6 (2010) 1705.
8. M. Moravej and D. Mantovani, *Int. J. Mol. Sci*., 12 (2012) 4250.
9. X.W. Liu, J.K. Sun, Y.H. Yang, Z.J Pu and Y.F. Zheng, *Mater. Lett*., 161 (2015) 53.
10. L. Rink, Zinc in Human Health, Ios Press, Amsterdam, 2011.
11. P. Trumbo , A. A. Yates , S. Schlicker and M. Poos , *J. Am. Diet. Assoc*., 101 (2001) 294.
12. B. Hennig , M. Toborek and C. J. McClain , *Nutrition*, 12(1996) 711.
13. D. Vojtech, J. Kubasek, J. Serak and P. Novak, *Acta. Biomater*., 7 (2011) 3515.
14. J. Kubasek and D. Vojtech, *Proc. Metal.*, 5 (2012) 23.
15. J.H. Wang, J.F. Huang, X.P. Su and C.J. Wu, *Mater. Design*, 38 (2012) 133.
16. Z.L. Liu, D. Qiu, F. Wang, J. A. Taylor and M.X. Zhang, *Acta Mater*., 79 (2014) 315.
17. Z.L. Liu, R.Q. Li, R.P. Jiang, X.Q. Li and M.X. Zhang, *J. Alloys Compd*., 687(2016) 885.
18. X.W Liu, J.K Sun, K.J Qiu, Y.H Yang, Z.J Pu, L. Li and Y.F Zheng, *J. Alloys Compd*., 664 (2016) 444.
19. T.K. Ha, J.R. Son, W.B. Lee, C.G. Park and Y.W. Chang, *Mater. Sci. Eng. A*, 307 (2001) 98.
20. G. Pürçek, *J. Mater. Process. Technol*., 169 (2005) 242.
21. G. Hercz, D. L Andress, H. G Nebeker,. J. H Shinaberger, D. J Sherrard and J. W Coburn, *J. Kidney. Dis*., 11(1) (1988) 70.
22. E. M. Gacek, A. L. Babb, D. A. Uvelli, D. L. Fry and B. H. Scribner, Asaio J. 25(1979) 409
23. G. Dunea, S.D. Mahurkar, B. Mamdani and E.C. Smith, *Ann. Intern. Med*., 88 (1978) 502.
24. D.M. Crapper, Aluminum and Alzheimer's disease. Neurobiology of aging 7. (1986)525.
25. C. Wang, H.T. Yang, X. Li and Y.F. Zheng, *J. Mater. Sci. Technol*., 32 (2016) 909.
26. F. Witte, N. Hort, C. Vogt, S. Cohen, K. U. Kainer, R. Willumeit and F. Feyerabend, *Curr. Opin. Solid. State. Mater. Sci*., 12 (2008) 63.
27. G. Eddy, J. Poinern, S. Brundavanam and D. Fawcett, *Am. J. Biomech. Eng*., 2 (2012) 218.
28. Y.F. Zheng, X.N. Gu and F. Witte, *Mat. Sci. Eng. A*., 77 (2014) 1.
29. D.I. Mario Carlo, G. Huw, G. Omer, P. Nicolas, V. Jan, B. Marc, D. Koen, H.Bernhard, R. Roland, K. Victor, I. Charles and E. Raimund, *J. Interv. Cardiol*., 17 (2004) 391.
30. W.B Zhang, Y.H Shen, H.B Pan, K.L Lin, X.G Liu, B. W Darvell, W.W. Lu, J. Chang, L.F Deng, D.P Wang and W.H Huang, *Acta. Biomater*., 7 (2011) 800.
31. Y. Liu, C. Geng, Y.K Zhu and X. Chen, *J. Alloys Compd*., 695 (2017) 443.
32. ASTM-G31-72: Standard Practice for Laboratory Immersion Corrosion Testing of Metals. Annual Book of ASTM Standards (2004).
33. H.Y. Li, Z.G. Li, Y. Liu and H.F. Jiang, *J. Alloys Compd*., 592 (2014) 127.
34. P. Vanysek, Electrochemical series. CRC handbook of chemistry and physics, 87 (1998).
35. E. Abd, E.E.Aal, *Corros. Sci*., 48 (2006) 343.
36. S.Thomas, N. Birbilis, M. S.Venkatraman and I. S. Cole, *J. Sci. Eng*., 68 (2012) 015009-1.
37. H. Gong, K. Wang, R. Strich and J.G. Zhou, *J. Biomed. Mater. Res. B: Appl. Biomater*., 103 (2015)1632.
38. J.Lévesque, H. Hermawan, D. Dubé and D. Mantovani, *Acta Biomater*., 4 (2008) 284.
39. X.G. Zhang, Corrosion and Electrochemistry of Zinc. Springer Science & Business Media, Berlin, Germany, 2013.
40. T. Falk, J.E. Svensson and L.G. Johansson, *J. Electrochem. Soc*., 145 (1998) 2993.
41. P.D.L. Neto, A.N. Correia, R.P. Colares and W.S. Araujo, *J. Braz. Chem. Soc*., 18 (2007) 1164.
42. M. Natesan, G. Venkatachari and N. Palaniswamy, *Corros.Sci*., 48 (2006) 3584.
43. C. Leygraf and T. Graedel, Atmospheric Corrosion, John Wiley & Sons, Inc., 2000.
44. L.J. Yang, Y.F. Li, Y.H. Wei, L.F. Hou, Y.G. Li and Y. Tian, *Corros. Sci*., 52 (2010) 2188.
45. L.J. Yang, Y.M. Zhang, X.D. Zeng and Z.L. Song, *Corros. Sci.*, 59 (2012) 229.
46. Y. Liu, H.Y. Li and Z.G. Li, *Int. J. Electrochem. Sci*., 8 (2013) 7753.

47. R. Zandi Zand, K. Verbeken and A. Adriaens, *Int. J. Electrochem. Sci.*, 8 (2013) 548.
48. R. Zandi Zand, K. Verbeken and A. Adriaens, *Int. J. Electrochem. Sci.*, 7 (2012) 9592.